Experimental demonstration of frequency-agile terahertz metamaterials

HOU-TONG CHEN[1]*, JOHN F. O'HARA[1], ABUL K. AZAD[1], ANTOINETTE J. TAYLOR[1], RICHARD D. AVERITT[2], DAVID B. SHREKENHAMER[3] AND WILLIE J. PADILLA[3]

[1]Center for Integrated Nanotechnologies, Materials Physics & Applications Division, Los Alamos National Laboratory, Los Alamos, New Mexico 87545, USA
[2]Department of Physics, Boston University, 590 Commonwealth Avenue, Boston, Massachusetts 02215, USA
[3]Department of Physics, Boston College, 140 Commonwealth Avenue, Chestnut Hill, Massachusetts 02467, USA
*e-mail: chenht@lanl.gov

Published online: 13 April 2008; doi:10.1038/nphoton.2008.52

Metamaterials exhibit numerous novel effects[1–5] and operate over a large portion of the electromagnetic spectrum[6–10]. Metamaterial devices based on these effects include gradient-index lenses[11,12], modulators for terahertz radiation[13–15] and compact waveguides[16]. The resonant nature of metamaterials results in frequency dispersion and narrow bandwidth operation where the centre frequency is fixed by the geometry and dimensions of the elements comprising the metamaterial composite. The creation of frequency-agile metamaterials would extend the spectral range over which devices function and, further, enable the manufacture of new devices such as dynamically tunable notch filters. Here, we demonstrate such frequency-agile metamaterials operating in the far-infrared by incorporating semiconductors in critical regions of metallic split-ring resonators. For this first-generation device, external optical control results in tuning of the metamaterial resonance frequency by ∼20%. Our approach is integrable with current semiconductor technologies and can be implemented in other regions of the electromagnetic spectrum.

Electromagnetic metamaterials are structured composites with patterned metallic subwavelength inclusions. These mesoscopic systems are built from the bottom up, at the unit cell level, to yield specific electromagnetic properties. Individual components respond resonantly to the electric, magnetic or both components of the electromagnetic field. In this way electromagnetic metamaterials can be designed to yield a desired response at frequencies from the microwave through to the near visible[6–10]. Importantly, additional design flexibility is afforded by the judicious incorporation of naturally occurring materials within or as part of the metamaterial elements. Specifically, hybrid metamaterial composites result when the properties of a natural material, for example, semiconductors, strongly couple with the resonance of a metamaterial element. The resulting hybrid metamaterials will still exhibit 'passive' properties (such as a negative electric response, negative index or gradient index), as determined by the patterning of the metamaterial elements. However, the aforementioned coupling engenders control of the passive metamaterial response by means of an external stimulus of the natural material response (such as photoconductivity, nonlinearity, gain). For example, amplitude control has been demonstrated through carrier injection[13,14] or depletion[15] in a semiconductor substrate, both of which shunt the capacitive region of the metamaterial elements. However, this simple approach, where the entire capacitive region is continuously covered with semiconductor, is insufficient to tune the resonance frequency.

To achieve frequency tunability, due consideration must be given to the incorporation of the semiconductor into the metamaterial elements. We describe hybrid metamaterials where precise patterning of semiconductors permits frequency tuning of the metamaterial resonance on photoexcitation. Our results represent an important initial step towards extending the spectral range over which a specific metamaterial device can operate, in addition to enabling the implementation of new device concepts.

There have been some efforts to realize frequency-tunable metamaterials[17–21], most of which have been demonstrated in the microwave frequency region. However, it should be noted that these designs only control the resonant properties of one or a handful of individual metamaterial elements. Thus, these techniques are not suitable at terahertz (THz) and higher frequencies, where the entire metamaterial composite may have more than 1×10^4 unit cells and monolithic integration of the tuning elements is important.

In Fig. 1a we show a scanning electron microscopy (SEM) image of the unit cell of a frequency-tunable THz metamaterial. It is a variant of previously demonstrated designs[22–24] that exhibit a Lorentz-like resonant response described by an effective complex permittivity $\varepsilon(\omega) = \varepsilon_1 + i\varepsilon_2$, where ε_1 and ε_2 are the real and imaginary parts, respectively. The split gap at the centre of the unit cell can be thought of as a capacitor, where charge accumulates on resonance. By constructing the capacitor plates from a semiconductor such as silicon, we can control the conductivity in response to the photoexcitation of free charge carriers, thereby altering the effective size of the capacitor and tuning the capacitance, C. As the resonance frequency is strongly dependent on the capacitance, that is, $\omega_0 \sim (LC)^{-1/2}$, where L is the effective inductance of the split-ring resonators (SRRs), then ω_0 should shift monotonically to lower frequencies as the photoexcitation fluence increases.

The metamaterials were fabricated on a silicon-on-sapphire (SOS) wafer. The (100) silicon layer was 600 nm thick, with an intrinsic resistivity >100 Ω cm. The R-plane sapphire substrate was 530 μm thick. The planar metamaterial array was fabricated using standard photolithographic methods, consisting of electron-beam

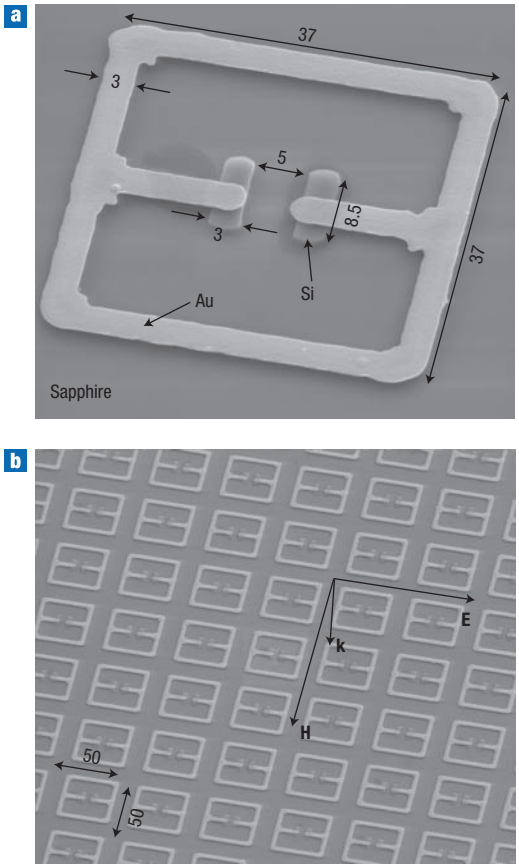

Figure 1 Scanning electron microscopy images of the frequency-tunable planar metamaterial. **a**, An individual unit cell. **b**, A periodically patterned square array. All dimensions are shown in micrometres and materials are indicated in the images. The polarization of the normally incident, linearly polarized THz radiation is also indicated in **b**. **H**: magnetic field; **E**: electric field.

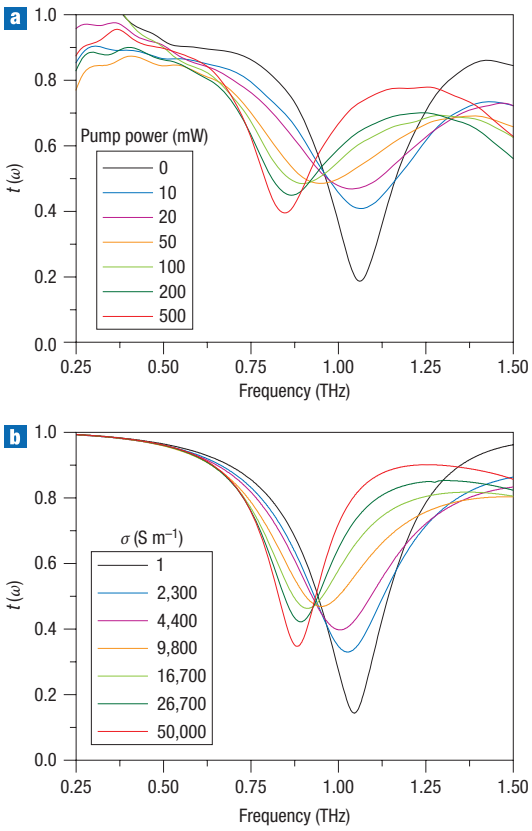

Figure 2 Terahertz electric-field transmission amplitude of the metamaterial shown in Fig. 1. **a**, Experimental measurements as a function of photoexcitation power. **b**, Numerical simulations as a function of silicon conductivity.

deposition of 10 nm of titanium and 200 nm of gold, and then a lift-off process. The metal stripes that had the split gaps lay along the primary flat orientation of the wafer, that is, 45° counterclockwise from the projection of the C-axis on the R-plane. Additional photoresist was patterned by photolithography to define the silicon regions (capacitor plates). The photoresist patterns and the metallic SRRs together served as a mask during the reactive ion etching (RIE) of the unwanted silicon regions. The final result (Fig. 1a,b) was the complete removal of the silicon layer except for regions under the metallic SRRs and at the silicon capacitor plates. By defining the SRRs on top of the silicon layer, we avoided any significant steps or discontinuities in the metallization.

We characterized the frequency-dependent electric response using THz time-domain spectroscopy (THz-TDS). The THz electric field was coherently measured following normal transmission through the metamaterial sample or a bare sapphire substrate serving as the reference. The THz electric field was oriented as shown in Fig. 1b to drive the electric resonance of the SRRs. The time-domain data were temporally windowed to eliminate the effects of multiple reflections within the sapphire substrate. Fourier transformation of the time-domain waveforms then provided the frequency-dependent THz electric-field amplitude and phase. Dividing the sample complex spectrum by the reference we obtained the transmission $t(\omega)$ and phase change $\Delta\phi(\omega)$ through the metamaterial. Photoexcitation of metamaterial silicon regions was achieved using optical-pump THz-probe (OPTP) spectroscopy[25]. The OPTP system provided amplified, ~30-fs, near-infrared laser pulses with a centre wavelength of 800 nm and a repetition rate of 1 kHz to optically excite charge carriers across the 1.12-eV bandgap of silicon[26]. The photocarrier lifetimes were orders of magnitude longer than the picosecond duration of the THz pulses. This enabled a quasi-steady-state characterization of the metamaterials as a function of the carrier density, which could be adjusted by changing the excitation fluence. In our measurements, photoexcitation occurred 10 ps before the arrival of the THz pulses. To ensure photoexcitation uniformity, the pump laser beam was expanded to a diameter of ~1 cm and two identical metal apertures of 3 mm diameter were placed in front of the sample and reference. The focused THz beam was approximately 3 mm in diameter at the sample.

The experimental results for the frequency-tunable metamaterial are shown in Fig. 2a. The transmitted THz electric-field amplitude with no photoexcitation is shown as the black curve. A transmission minimum $t(\omega) = 19\%$ occurs near resonance at 1.06 THz, whereas off-resonance transmission is ~90%. As the photoexcitation power increases (10–20 mW), the resonance initially weakens and broadens, showing little perceptible shift in frequency. On further increase in the excitation power (50–100 mW), the resonance continues to weaken and saturates at $t(\omega) = 49\%$, but now shifts to significantly lower frequencies. Increasing the excitation power

beyond 100 mW causes continued shifting to lower frequencies and also re-establishes the resonance strength and narrows the linewidth. At a photoexcitation power of 500 mW (a fluence of $\sim$0.5 mJ cm^{-2} or carrier density of $\sim 2.5 \times 10^{18}$ cm^{-3}) we achieved $t(\omega) = 40\%$ at 850 GHz (red curve). This represents a tuning range of 20% in the resonance frequency.

To explain the nature of the frequency tuning, we performed finite-element simulations using commercial software Microwave Studios by CST (ref. 27). We simulated a single cubic unit cell as shown in Fig. 1a, with the SRR located at the centre. The boundary conditions on faces parallel to the propagation vector **k** were set as perfect electric conductor or perfect magnetic conductor to approximate a transverse electromagnetic plane wave propagating through the periodic SRR array of the hybrid metamaterial sample or the reference substrate, as shown in Fig. 1b. We set the input and output ports on the top and bottom faces of the cubic unit cell in the air and sapphire, respectively, which minimizes Fresnel reflections at the back interface of the 530-μm-thick sapphire substrate. In simulations we used adaptive mesh refinement to ensure an accurate numerical solution with a short simulation time. The final mesh typically contained about 50,000 tetrahedrons, and the minimum edge length was about 0.013 μm. The simulation produced the frequency-dependent complex S-parameters and we focus here on the transmission $t(\omega) = |E_t(\omega)/E_i(\omega)| = |S_{21}(\omega)|$ normalized by a blank sapphire substrate, where $E_t(\omega)$ and $E_i(\omega)$ are the transmitted and incident fields, respectively. The gold regions were simulated as lossy metal with a conductivity of $\sigma_{gold} = 7 \times 10^6$ S m^{-1}, and the silicon underlying the metamaterials was modelled as a dielectric with $\varepsilon_{Si} = 11.7$ and $\sigma_{Si} = 1$ S m^{-1}. The sapphire substrate was modelled as a lossless dielectric with $\varepsilon_{sapphire} = 10.5$, the average value of ε along the ordinary and extraordinary axes[28]. The photoexcited silicon capacitor plates were simulated with $\varepsilon_{Si} = 11.7$ and a pump-power-dependent conductivity. We included 1-μm undercuts in the silicon located beneath the gold regions, an attribute of our sample caused by the RIE process. Finally, we accounted for the irregular geometry (rounded corners and chamfers of the fabricated structure) apparent in the SEM image of the metamaterial.

Simulation results are shown in Fig. 2b, and excellent agreement is observed both quantitatively and qualitatively when compared to the experimental measurements. We used a silicon conductivity value of $\sigma = 50{,}000$ S m^{-1} to simulate a photoexcitation power of 500 mW and found good agreement with experimental data. The excited charge-carrier density is proportional to the excitation power. However, the conductivity increases more slowly as there is a decrease in mobility with photoexcited carrier density due to increased electron–electron scattering. The conductivity values, specified in Fig. 2b, were found to be in reasonable agreement with Drude calculations for photoexcited silicon with the fluences specified in Fig. 2a.

The simulations support the observed experimental behaviour. For small values of silicon conductivity there is an initial damping of the resonance strength due to ohmic losses in the silicon plates, which weakens the resonance strength as shown in Fig. 2. Further, the small silicon conductivities are insufficient to enable charge accumulation, and the slight change in dielectric function on low fluence photoexcitation is not enough to alter the capacitance and shift the resonance frequency. This is similar to the results of previous studies[13,14] in which switchable THz metamaterials were created by incorporating semiconductor substrates. Here an even lower conductivity was required to completely switch off the resonance as a result of the substrate allowing current flow across the gaps of the SRRs. We emphasize, however, that in the previous studies[13–15] the injected carriers short-circuit the SRR

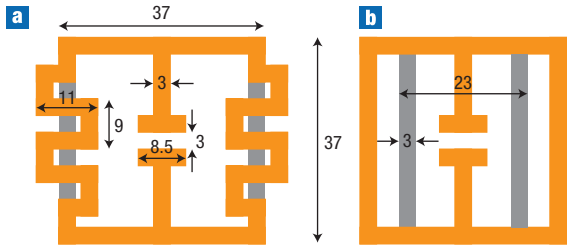

Figure 3 Schematic of inductively tuned metamaterial designs. **a**,**b**, The photoexcited silicon regions form parallel current paths through the meandering loop sections (**a**) and across the regular loop sections (**b**) to effectively modify the inductance of the SRRs. The metal and silicon regions are displayed in orange and grey, respectively. The dimensions are shown in micrometres.

capacitance. In the present work, the patterned semiconductor is an integral part of the metamaterial, that is, the SRR capacitor plates. As the conductivity increases, the resonance shifts to lower frequencies. At intermediate conductivity values, more charge accumulates on the silicon plates, yielding a redshift of the resonance. The damping remains strong, because current flow is still impeded by ohmic losses in the silicon. Finally, at high conductivity values, the silicon begins to behave more like a metal. The high charge carrier density imposes little resistance to current flow, allowing a smooth delivery of charge between the silicon and the metallic SRRs, thereby reducing damping. The charge readily accumulates in the silicon, contributing to the capacitance. Effectively, photoexcitation changes the size of the capacitor plates. We note that despite the reduction in oscillator strength for photoexcitation powers ranging between 20 mW and 100 mW, the resonance of the metamaterial indeed shifts to lower frequencies as expected, from 1.06 THz to 850 GHz, a tuning range of 20%. The simulated results show similar behaviour, with a tuning range of 16%. The slight discrepancies in frequency tunability and resonance linewidth between the experiment and simulation results are mainly due to imperfections in sample fabrication, which were not fully taken into account in the simulations.

For greater flexibility and with a view towards applications it would be ideal to have additional metamaterials that are tunable to higher frequencies on photoexcitation. In Fig. 3 we present simulated studies of two designs that accomplish this task and yield resonant responses in the THz frequency range. Unlike our previous sample, these designs use frequency tuning by altering the inductance L of the metamaterial element. The incorporation of the semiconductor regions shown in Fig. 3a and b will, under photoexcitation, reduce the loop length, thereby shifting the resonance to higher frequencies. In Fig. 4 we show the simulated transmission as a function of silicon conductivity for both metamaterial structures. The simulation results follow expectations: the resonances shift to higher frequencies with increasing semiconductor conductivity. As with our previous design in Fig. 1a, the resonance initially weakens as it shifts, but eventually recovers. Similar tunabilities are achievable; simulations show ω_0 increasing by 15% in Fig. 4a and 40% in Fig. 4b for the structures in Fig. 3a and b, respectively. However, it should be noted that the conductivity values needed to realize such tunabilities are one order of magnitude higher than those used in Fig. 2b. This results from the significant amount of current required to traverse the silicon regions to reduce the effective loop size. Thus the silicon conductivity has to be

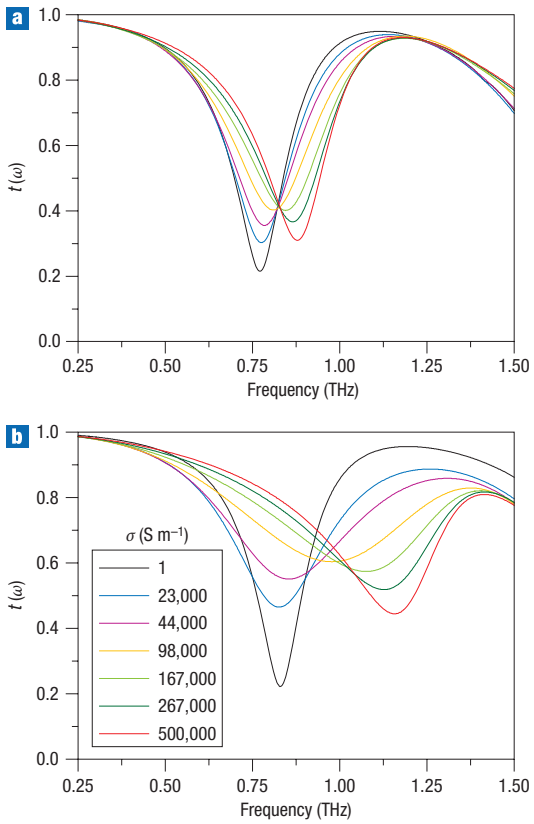

Figure 4 Simulated THz electric-field transmission amplitude of metamaterial designs presented in Fig. 3. a,**b**, Simulations of the structure of Fig. 3a (**a**) and the structure of Fig. 3b (**b**), both using the silicon conductivity values shown in the key.

comparable to that of gold, which is difficult to achieve by photoexcitation of silicon. In contrast, there is much less current travelling through the silicon regions used to construct the capacitor plates in Fig. 1. In any case, the simulated structures along with the experimentally demonstrated frequency-agile metamaterials (Figs 1 and 2) will be useful for the construction of future novel devices. The extended functionality offered by the hybrid metamaterials presented here will undoubtedly play a key role.

Received 5 December 2007; accepted 18 February 2008; published 13 April 2008.

References

1. Veselago, V. G. The electrodynamics of substances with simultaneously negative values of ε and μ. *Sov. Phys. Usp.* **10,** 509–514 (1968).
2. Shelby, R. A., Smith, D. R. & Schultz, S. Experimental verification of a negative index of refraction. *Science* **292,** 77–79 (2001).
3. Pendry, J. B. Negative refraction makes a perfect lens. *Phys. Rev. Lett.* **85,** 3966–3969 (2000).
4. Fang, N., Lee, H., Sun, C. & Zhang, X. Sub-diffraction-limited optical imaging with a silver superlens. *Science* **308,** 534–537 (2005).
5. Schurig, D. *et al.* Metamaterial electromagnetic cloak at microwave frequencies. *Science* **314,** 977–980 (2006).
6. Wiltshire, M. C. K. *et al.* Microstructured magnetic materials for RF flux guides in magnetic resonance imaging. *Science* **291,** 849–851 (2001).
7. Smith, D. R., Padilla, W. J., Vier, D. C., Nemat-Nasser, S. C. & Schultz, S. Composite medium with simultaneously negative permeability and permittivity. *Phys. Rev. Lett.* **84,** 4184–4187 (2000).
8. Yen, T. J. *et al.* Terahertz magnetic response from artificial materials. *Science* **303,** 1494–1496 (2004).
9. Soukoulis, C. M., Linden, S. & Wegener, M. Negative refractive index at optical wavelengths. *Science* **315,** 47–49 (2007).
10. Shalaev, V. M. Optical negative-index metamaterials. *Nature Photon.* **1,** 41–48 (2007).
11. Smith, D. R., Mock, J. J., Starr, A. F. & Schurig, D. Gradient index metamaterials. *Phys. Rev. E* **71,** 036609 (2005).
12. Greegor, R. B. *et al.* Simulation and testing of a graded negative index of refraction lens. *Appl. Phys. Lett.* **87,** 091114 (2005).
13. Padilla, W. J., Taylor, A. J., Highstrete, C., Lee, M. & Averitt, R. D. Dynamical electric and magnetic metamaterial response at terahertz frequencies. *Phys. Rev. Lett.* **96,** 107401 (2006).
14. Chen, H.-T. *et al.* Ultrafast optical switching of terahertz metamaterials fabricated on ErAs/GaAs nanoisland superlattices. *Opt. Lett.* **32,** 1620–1622 (2007).
15. Chen, H.-T. *et al.* Active terahertz metamaterial devices. *Nature* **444,** 597–600 (2006).
16. Alù, A. & Engheta, N. Guided modes in a waveguide filled with a pair of single-negative (SNG), double-negative (DNG), and/or double-positive (DPS) layers. *IEEE Trans. Microwave Theory Techniques* **52,** 199–210 (2004).
17. Gil, I. *et al.* Varactor-loaded split ring resonators for tunable notch filters at microwave frequencies. *Electron. Lett.* **40,** 1347–1348 (2004).
18. Gil, I., Bonache, J., García-García, J. & Martín, F. Tunable metamaterial transmission lines based on varactor-loaded split-ring resonators. *IEEE Trans. Microwave Theory Techniques* **54,** 2665–2674 (2006).
19. Lim, S., Caloz, C. & Itoh, T. Metamaterial-based electronically controlled transmission-line structure as a novel leaky-wave antenna with tunable radiation angle and beamwidth. *IEEE Trans. Microwave Theory Techniques* **52,** 2678–2690 (2004).
20. Kim, H., Ho, S.-J., Choi, M.-K., Kozyrev, A. B. & van der Weide, D. W. Combined left- and right-handed tunable transmission lines with tunable passband and 0° phase shift. *IEEE Trans. Microwave Theory Techniques* **54,** 4178–4184 (2006).
21. Degiron, A., Mock, J. J. & Smith, D. R. Modulating and tuning the response of metamaterials at the unit cell level. *Opt. Express* **15,** 1115–1127 (2007).
22. Schurig, D., Mock, J. J. & Smith, D. R. Electric-field-coupled resonators for negative permittivity metamaterials. *Appl. Phys. Lett.* **88,** 041109 (2006).
23. Padilla, W. J. *et al.* Electrically resonant terahertz metamaterials: Theoretical and experimental investigations. *Phys. Rev. B* **75,** 041102(R) (2007).
24. Chen, H.-T. *et al.* Complementary planar terahertz metamaterials. *Opt. Express* **15,** 1084–1095 (2007).
25. Averitt, R. D. & Taylor, A. J. Ultrafast optical and far-infrared quasiparticle dynamics in correlated electron materials. *J. Phys. Condens. Matter.* **14,** R1357–R1390 (2002).
26. Sze, S. M. *Physics of Semiconductor Devices* (Wiley, Hoboken, New Jersey, 2007).
27. CST Studio Suite 2006B <http://www.cst.com>.
28. Grischkowsky, D., Keiding, S., van Exter, M. & Fattinger, C. Far-infrared time-domain spectroscopy with terahertz beams of dielectrics and semiconductors. *J. Opt. Soc. Am. B* **7,** 2006–2015 (1990).

Acknowledgements

We acknowledge support from the Los Alamos National Laboratory LDRD Program. This work was performed, in part, at the Center for Integrated Nanotechnologies, a US Department of Energy, Office of Basic Energy Sciences nanoscale science research centre operated jointly by Los Alamos and Sandia National Laboratories. Los Alamos National Laboratory, an affirmative action/equal opportunity employer, is operated by Los Alamos National Security, LLC, for the National Security administration of the US Department of Energy under contract DE-AC52-06NA25396. D.B.S. and W.J.P. acknowledge support from the Office of Naval Research (ONR), grant N000140710819. H.-T.C. would also like to acknowledge E. Akhadov for the SEM imaging, and stimulating discussions with K. Burch and A. Findikoglu.

Author information

Reprints and permission information is available online at http://npg.nature.com/reprintsandpermissions/. Correspondence and requests for materials should be addressed to H.-T.C.